

# Direct Numerical Simulation of Turbulent Flow Using Hyperbolic Moment Methods

L. Ivan\* and W. Kaufmann\*\*

Corresponding author: lucian.ivan@cnl.ca

\* Canadian Nuclear Laboratories, Chalk River, ON, Canada, K0J 1J0.

\*\* University of Ottawa, Ottawa, ON, Canada, K1N 6N5.

**Abstract:** Moment-based methods derived from gaskinetic theory using an entropy-maximization formulation lead to a set of first-order hyperbolic balance laws with stiff relaxation source terms for the description of viscous fluid flow. Despite offering a viable alternative to the Navier-Stokes (NS) equations, moment-based methods do not appear to have been considered for the direct numerical simulation (DNS) of turbulent flow. A key enabler in this work for performing novel DNS studies with hyperbolic moment models has been the development and implementation of a recently-proposed third-order, coupled space-time discontinuous-Galerkin Hancock method with an efficient locally-implicit treatment for stiff source terms. The use of hyperbolic equations to model turbulent viscous flow provides several computational advantages over employing the NS equations: i) to offer a physics-based model with finite propagation speeds; ii) to avoid the discretization of elliptic-type operators, which can be associated with more severe time-step restrictions and violation of the maximum principle; and iii) to reduce the sensitivity to grid irregularities induced by gradient reconstructions. A key advantage of describing viscous flows with moment-based models derived from gaskinetic theory is that they extend the model validity beyond the continuum regime of the fluid flow. This novel capability of our modelling framework paves the way to investigate essential and long-lasting questions related to turbulent flows: can there be non-continuum effects present at Kolmogorov scale for turbulent flows? If so, how relevant is it that these effects are accounted for? Computational studies using the benchmark Taylor-Green vortex problem with Mach and Reynolds numbers equal to 0.1 and 1,600, respectively, are included here to demonstrate the predictive capabilities of the hyperbolic moment-model for DNS of turbulent flow. Although the moment-based solution approaches closely the reference NS result obtained with a spectral method, some differences are still observed even when using a fine computational grid with  $512^3$  elements.

*Keywords:* Turbulence Modeling, Direct Numerical Simulation, Moment-Based Methods, Discontinuous-Galerkin Hancock Scheme.

## 1 Introduction

Turbulence is a phenomenon of fundamental importance to myriad flows. The traditional understanding for the past century is that all turbulence scales occur in a continuum regime [1], and therefore, turbulence is almost exclusively studied at the hydrodynamic (continuum) level. However, this established assumption has been more recently revisited in relation to certain flows [2], and scale analysis arguments suggest that non-continuum effects could play an important role at the small scale motion of turbulence flows, with the smallest of these being the Kolmogorov scales [1]. In fact, there are cases of practical interest [2, 3] in which the Kolmogorov length and time scales can be within one-to-two orders of magnitude of the mean free path,  $l_{\text{mfp}}$ , and the mean collision time,  $t_{\text{mct}}$ , respectively. For a gas flow with a turbulent Mach number,  $M_t$ , and a turbulent Reynolds number,  $Re_t$ , a scaling analysis [2] shows that the ratio of the Kolmogorov length scale,

$\eta \equiv \left(\frac{\nu^3}{\epsilon}\right)^{1/4}$ , to the mean free path, and the ratio of the Kolmogorov time scale,  $\tau \equiv \left(\frac{\nu}{\epsilon}\right)^{1/2}$ , to the mean collision time vary as

$$\begin{aligned} \frac{\eta}{l_{\text{mfp}}} &\sim \frac{\text{Re}_t^{1/4}}{M_t} \text{ and} \\ \frac{\tau}{t_{\text{mct}}} &\sim \frac{\text{Re}_t^{1/2}}{M_t^2}, \end{aligned} \tag{1}$$

respectively. Here,  $\nu$  is the kinematic viscosity and  $\epsilon = -\frac{dk}{dt}$  is the dissipation rate given by the rate of change of turbulent kinetic energy,  $k$ . Assuming a high-speed gas flow with  $M_t = 1$  and  $\text{Re}_t = 10,000$ , the first and second ratios in Eq. 1 are approximately 10 and 100, respectively [2]. In such instances, studying turbulence and energy exchange at the molecular kinetic level may offer new physical insights.

In terms of the spatial scales, the situation can be analyzed through the Knudsen number [4],  $\text{Kn} = \frac{l_{\text{mfp}}}{L_{\text{char}}}$ , where  $L_{\text{char}}$  is a characteristics length scale of the fluid mechanical system, which, in the case of turbulent scales, is related to the eddy size [5]. The Knudsen number value is a good indicator of what kind of local flow conditions are encountered. The simplest situation occurs when  $\text{Kn} \lesssim 0.01$  since the continuum hypothesis is assumed valid. In this case, the flow is well described by the Navier-Stokes (NS) equations. However, the condition corresponds to free molecular flow for  $\text{Kn} \gtrsim 10$ , and a molecular level description such as the full kinetic (Boltzmann) equation is well suited. Direct simulation Monte-Carlo (DSMC) method [3] is a suitable technique for solving Boltzmann equation in this flow regime. Between the continuum and free molecular flow limits, there is a transition regime, i.e.,  $0.01 \lesssim \text{Kn} \lesssim 10$ , where the NS equations, which are based on the continuum fluid assumption, cease to be valid, and the alternative, physically valid option provided by DSMC is typically computationally prohibitive.

Performing an analysis of the Knudsen number based on the Kolmogorov scale,  $\eta$ , the so-called ‘‘micro-structure Knudsen number’’,  $\text{Kn}_\eta$ , can be expressed as a function of  $M_t$  and  $\text{Re}_t$  as [5]

$$\text{Kn}_\eta = \sqrt{\frac{\pi\gamma}{2}} \left( \frac{M_t}{\text{Re}_t^{1/4}} \right), \tag{2}$$

where  $\gamma$  is the gas adiabatic index. The weak dependency on turbulent Reynolds number (i.e.,  $-1/4$  power) suggests that the continuum hypothesis will generally hold over a wide range of Reynolds numbers. Nevertheless, non-continuum effects present at Kolmogorov scale for turbulent flows are also possible, according to Eq. 2, for flows of practical interest, and their investigation requires computational models that account for non-equilibrium effects.

## 2 Scope of Work

Recently, Gallis *et al.* [3] provided the first demonstration that molecular-level methods based on gas kinetic theory and molecular chaos can simulate turbulence and its decay, by applying DSMC to simulate the Taylor-Green vortex (TGV) flow [6] at Mach and Reynolds numbers of 0.3 and 450, respectively. This simulation required eight billion cells ( $2,000^3$ ) and a total of 0.24 trillion particles. Although Gallis *et al.* [3] successfully demonstrated that the DSMC solution recovered the NS result, the simulation used 0.5 million cores on the Sequoia System (IBM Gene/Q processors), or about a third of this petascale supercomputer, for 500h (i.e., 21 days). This result is descriptive of the high computational cost associated with the application of DSMC method in the continuum flow regime, even for a modest Reynolds number.

More recently, Gallis *et al.* [7] investigated a range of Mach and Reynolds numbers for the TGV problem using both the DSMC method for noncontinuum molecular gas dynamics and the direct numerical simulation (DNS) of turbulent flow described by the NS equations. For the Mach and Reynolds numbers examined, it appears the two methods produce the same energy decay, although the DSMC flows evolve along trajectories in phase space that are different from but basically similar to those of DNS. In a very recent and revolutionary paper, McMullen *et al.* [8] have provided evidence based on studies with the TGV that deviations between the spectra decay generated by the molecular-gas-dynamics and NS simulations occur, thereby concluding that the NS equations are not guaranteed to describe the smallest scales of gas turbulence for any positive Knudsen number. These precursor studies clearly illustrate the significance of elucidating the role of non-equilibrium

effects in canonical turbulence situations, which could lead to fundamental changes in the understanding of turbulence.

Despite its relative success for a range of relatively lower Reynolds number cases, DSMC is an expensive technique for resolving phenomena from molecular to hydrodynamic (continuum) length scales in gas flows as it uses probabilistic Monte Carlo simulation to solve the Boltzmann equation. Alternatively, the moment-based methods [9, 10] used in the present work lead to a set of first-order hyperbolic balance laws with stiff relaxation source terms for the description of turbulent viscous, compressible fluid flow, that extends over the continuum limit of flow regimes into the transitional domain. Despite offering a viable alternative to the NS equations, moment-based methods do not appear to have been considered for the DNS of turbulent flow. Thus, the investigation pursued here is novel and a first-of-a-kind in its approach.

Moment-based models derived from the gaskinetic theory can be used for the prediction of continuum and non-equilibrium flows, and offer computational advantages over other fluid-flow models such as the NS equations. Moment models are described by first-order hyperbolic partial differential equations (PDEs), thereby avoiding the complications raised by elliptic-type operators. For instance, they are less sensitive to grid irregularities due to their hyperbolic nature [11]. Furthermore, they allow for an additional degree of accuracy over second-order PDEs for an equivalent number of degrees of freedom.

The diatomic extension [12] for the ten-moment (Gaussian) closure [10] offers a viable model for viscous, compressible fluid flow that extends over the continuum limit of flow regimes into the transitional domain. However, the absence of heat flux in the Gaussian system limits its range of application [10]. Moreover, the presence of stiff local source terms requires a careful numerical treatment in the solution procedure. A key enabler in this work for performing novel DNS studies with the hyperbolic ten-moment model [12] (see Sect. 3.2 for details) has been the development and implementation of a recently proposed third-order, coupled space-time discontinuous-Galerkin Hancock (DGH) scheme with an efficient locally implicit treatment for stiff source terms [13, 14]. To the best of our knowledge, this is the first application of hyperbolic moment-models to the DNS of turbulent flow.

This paper is organized as follows. In Sect. 3, after a brief review of the moment-closure procedure and the class of maximum-entropy closure, the Gaussian closure system used for performing DNS of turbulent flow is presented. The extension [12] of the ten-moment Gaussian closure for diatomic gases leads to a hyperbolic system of eleven PDEs with stiff relaxation source terms, which are used here. Section 4 provides details about the discretization procedure used in the present work to solve the hyperbolic model for viscous, compressible fluid flow at large computational scale. Computational DNS studies performed with the aforementioned moment-closure procedure for the decaying turbulence produced by the TGV are presented in Sect. 5. Finally, some conclusions concerning the applicability of moment closure approach for the DNS of turbulent flow are drawn in Sect. 6.

## 3 Hyperbolic Governing Equations for the Direct Numerical Simulation of Turbulent Flow

### 3.1 Moment-Closure Methods

Moment closures follow from the kinetic theory of gases [15]. In this theory, the particle nature of a gas is not ignored, however, the individual evolution of each atom or molecule is not directly tracked. Rather, a distribution function,  $\mathcal{F}(x_i, v_i, t)$ , is defined which gives the phase-space density of particles of a single-species gas at a position,  $x_i$ , with velocity,  $v_i$ , at a time,  $t$ .

Traditional macroscopic variables can be computed by taking moments of  $\mathcal{F}$ . This is done by multiplying the distribution function by an appropriately chosen weight and integrating over all velocity space. For example, the spatial number density of particles is given by

$$n(x_i, t) = \int_{\infty}^{\infty} \mathcal{F} dv_i = \langle \mathcal{F} \rangle .$$

Here, the weight is simply taken as the constant of unit value, and the compact notation,  $\langle \cdot \rangle$ , denotes

integration over all three dimensions of velocity space. Other commonly used moments are

$$n u_i = \langle v_i \mathcal{F} \rangle, \quad n P_{ij} = \langle c_i c_j \mathcal{F} \rangle, \quad n Q_{ijk} = \langle c_i c_j c_k \mathcal{F} \rangle.$$

Here,  $u_i$  is the average particle velocity at a point and time. This allows the difference between individual particle velocities and the local average to be defined as  $c_i = v_i - u_i$ . The variance-covariance tensor,  $P_{ij}$ , represents the pressure tensor and describes the spread of particle velocities and the correlation between individual components of the particle velocities. This tensor is symmetric, with six distinct entries. For a monatomic gas, it is related to the traditional thermodynamic pressure with  $p = P_{ii}/3$ , and to the deviatoric (viscous) stress tensor with  $\tau_{ij} = p\delta_{ij} - P_{ij}$ . The third-order tensor,  $Q_{ijk}$ , is the generalized skewness tensor and represents asymmetries of the distribution function. Moments of arbitrarily high order can be taken, however, the interpretation of their physical meaning becomes harder.

For a fluid with particles of the same kind, the evolution of the particle distribution function is governed by a kinetic equation,

$$\frac{\partial \mathcal{F}}{\partial t} + v_i \frac{\partial \mathcal{F}}{\partial x_i} + \frac{\partial}{\partial v_i} (a_i \mathcal{F}) = S, \quad (3)$$

which is the well-known Boltzmann equation of gas dynamics [4]. Here,  $a_i$  is the particle acceleration due to effects such as drag or external fields, which is neglected in the present work. The local source term on the right-hand side is chosen to be appropriate for the situation of interest. For example, if the right-hand side,  $S$ , is taken to be the Boltzmann collision integral this term models the effects of inter-particle collisions on the distribution function.

Equation (3) is extremely flexible and can be adapted to model a very wide range of situations, however it is extremely high dimensional. The equation exists in three space dimensions, three velocity dimensions, and time. Any solution through a direct discretization would be extremely expensive and limited to trivially small problems. Fortunately, a lower-dimensional equation can be derived for a given macroscopic statistical moment of the  $\mathcal{F}$ . For example, given a weight function,  $W$ , that corresponds to an arbitrary moment,  $U = \langle W \mathcal{F} \rangle$ , a moment of Eq. (3) gives

$$\frac{\partial}{\partial t} \langle W \mathcal{F} \rangle + \frac{\partial}{\partial x_i} \langle v_i W \mathcal{F} \rangle = - \left\langle a_i \mathcal{F} \frac{\partial W}{\partial v_i} \right\rangle + \langle W S \rangle. \quad (4)$$

For many situations, all terms on the right-hand side of Eq. (4) can be evaluated in closed form and yield algebraic expressions. However, on the left-hand side, one sees that the time evolution of an arbitrary moment will always depend on the divergence in space of a moment of one order higher. This will lead to an infinite set of coupled equations and is obviously impractical.

Any technique used to close the infinite set of equations resulting from Eq. (4) is known as a *moment closure*. The most popular way of doing this is by restricting the allowed form of  $\mathcal{F}$  to have a prescribed form in terms of a finite number of closure coefficients. In doing so, the number of degrees of freedom is restricted and the moment equations naturally close.

Though many techniques exist for closing the form of  $\mathcal{F}$ , in this work, an entropy maximization principle is used [9, 16, 17]. In this method, a set of moments of interest are chosen, then  $\mathcal{F}$  is restricted to be whatever has the highest entropy while being consistent with the known moments. The prescribed form for a maximum-entropy closure is given by  $\mathcal{F} = e^{\boldsymbol{\alpha}^\top \mathbf{W}}$ , where the number of free parameters,  $\boldsymbol{\alpha} = [\alpha_1, \alpha_2, \dots, \alpha_N]^\top$  is the same as the number of desired macroscopic properties,  $\mathbf{U}$ . The closure coefficients are the Lagrange multipliers obtained from the constrained entropy-maximization problem. Moment closures of this type yield an expanded sets of first-order hyperbolic balance-laws for the evolution of the chosen moments,  $\mathbf{U}$ , which can be expressed as

$$\frac{\partial \mathbf{U}}{\partial t} + \frac{\partial \mathbf{F}_i}{\partial x_i} = \mathbf{S}, \quad (5)$$

where  $\mathbf{F}_i = \langle v_i \mathbf{W} \mathcal{F} \rangle$  is the flux dyad and  $\mathbf{S} = \langle \mathbf{W} \frac{\delta \mathcal{F}}{\delta t} \rangle$  is the vector of local source terms. There are also strong physical arguments as to why models derived in this fashion should provide accurate predictions [9, 10].

The traditional Euler equations are provided by the five-moment closure with the weight vector  $\mathbf{W}_5 = [m, mv_i, mv_i v_i]^\top$ . Another low-order member of this hierarchy is the ten-moment Gaussian model which is

derived using  $\mathbf{W}_{10} = [m, mv_i, mv_i v_j]^\top$ . This Gaussian closure model is well suited for describing viscous, adiabatic flow, and is used in the present study.

### 3.2 Ten-moment (Gaussian) Closure Model for Viscous, Compressible Fluid Flow

One successful member of the maximum-entropy hierarchy for gases is the ten-moment, or Gaussian, moment model, which was first proposed by Levermore and Morokoff [10] for a monatomic gas. This model results from choosing the number density, the local average velocity, and the velocity variance-covariance tensor as the moments of interest. The maximum-entropy theory [9] leads to a distribution function of the form

$$\mathcal{F}_G = \frac{n}{(2\pi)^{\frac{3}{2}} (\det \Theta_{ij})^{\frac{1}{2}}} \exp\left(-\frac{1}{2} \Theta_{ij}^{-1} c_i c_j\right), \quad (6)$$

where  $\Theta_{ij} = P_{ij}/\rho$  is an anisotropic “temperature” tensor. Insertion of this assumed form into Eq. (4) gives a set of three tensor equations for ten independent fields,

$$\frac{\partial n}{\partial t} + \frac{\partial}{\partial x_k} n u_k = 0, \quad (7)$$

$$\frac{\partial}{\partial t} n u_i + \frac{\partial}{\partial x_k} n (u_i u_k + \Theta_{ik}) = 0, \quad (8)$$

$$\frac{\partial}{\partial t} n (u_i u_j + \Theta_{ij}) + \frac{\partial}{\partial x_k} n (u_i u_j u_k + u_i \Theta_{jk} + u_j \Theta_{ik} + u_k \Theta_{ij}) = S_G. \quad (9)$$

This first-order hyperbolic model for viscous compressible gases can be seen as an alternative to the compressible Navier-Stokes equations. In fact, by allowing for anisotropic temperatures, the ten-moment model can remain accurate for significant departures from local thermodynamic equilibrium, in cases for which the Navier-Stokes equations lose validity. This model has proven successful in predictive viscous flows both in and out of thermodynamic equilibrium [18, 19, 20, 21]. In addition to being accurate and efficient, the first-order nature of the resulting equations has been shown to make numerical solutions less sensitive to grid quality [11]. This is especially advantageous for practical situations with complex geometry for which high-quality grid generation is very difficult.

As previously mentioned, the Gaussian closure was originally derived for a monatomic gas with only three translational degrees of freedom, and no internal degrees of freedom associated with rotational and vibrational modes. Later on, Hittinger [12] extended the formulation to account for the rotational energy that can be present in internal degrees of freedom for a diatomic gas. In this case, assuming a “dumbbell” model of a diatomic molecule, the total velocity distribution for the diatomic gas becomes

$$\mathcal{G}_D(x_i, v_i, \omega, t) = \frac{n^2 I}{(2\pi)^{5/2} (\det \Theta)^{1/2} p} \left(\frac{T}{T_{\text{rot}}}\right) \exp\left(-\frac{1}{2} \Theta_{ij}^{-1} c_i c_j\right) \exp\left(-\frac{1}{2} R \omega^2\right), \quad (10)$$

where the rotational velocities are assumed statistically independent of each other and of the translational velocities,  $I$  is a moment of inertia, and  $\omega$  is the magnitude of an angular velocity vector defined in an appropriately chosen coordinate system about the center of mass of the diatomic molecule (see [12] for details). Making an analogy to the translational degrees of freedom and the associated translational temperature,  $T$ , a rotational temperature,  $T_{\text{rot}}$ , can be defined for the temperature of rotational degrees of freedom. The variable  $R$  is given by  $R = \frac{nI}{p} \left(\frac{T}{T_{\text{rot}}}\right)$ . Aside from time, this distribution function is now defined in seven-dimensional space consisting of three position coordinates, three translational velocity components, and an angular velocity dimension. In this case, moments of the distribution function are achieved by integrating not only over all velocity space, but also over the angular velocity space. Though the rotational and translational temperatures need not be equal in general, they will become equal only when the gas is in thermodynamic equilibrium.

The final form of the Gaussian-moment system used in the present work to describe viscous, compressible

fluid flow of diatomic gas is given by [12]

$$\begin{aligned}
\frac{\partial \rho}{\partial t} + \frac{\partial}{\partial x_k} (\rho u_k) &= 0, \\
\frac{\partial}{\partial t} (\rho u_i) + \frac{\partial}{\partial x_k} (\rho u_i u_k + P_{ik}) &= 0, \\
\frac{\partial}{\partial t} (P_{ij} + \rho u_i u_j) + \frac{\partial}{\partial x_k} (\rho u_i u_j u_k + u_i P_{jk} + u_j P_{ik} + u_k P_{ij}) \\
&= -\frac{3P_{ij} - P_{kk}\delta_{ij}}{3\tau_t} - \frac{2(P_{kk} - 3E_{\text{rot}})}{15\tau_r} \delta_{ij}, \\
\frac{\partial E_{\text{rot}}}{\partial t} + \frac{\partial}{\partial x_k} (u_k E_{\text{rot}}) &= -\frac{3E_{\text{rot}} - P_{kk}}{5\tau_r}.
\end{aligned} \tag{11}$$

Here, the relaxation times can be related to the gas viscosities with

$$\tau_t = \frac{\mu}{p}, \quad \tau_r = \frac{15\mu_B}{4p}, \tag{12}$$

where  $\mu$  is the molecular fluid viscosity,  $\mu_B$  is the bulk viscosity, and  $p = (P_{ii} + 2E_{\text{rot}})/5$ . In comparison to a monatomic gas, Eq. 12 for a diatomic gas with rotational degrees of freedom introduce an advection-relaxation equation for the rotational energy density of the gas,  $E_{\text{rot}}$ . Furthermore, there is an additional relaxation on the time scale  $\tau_r$  of the generalized pressure tensor to equilibrium. This model provides a description of diatomic ideal gas at moderate temperatures in which the heat transfer is negligible.

## 4 Discretization Procedure

In addition to their physical modelling advantages, moment-based methods are highly desirable numerically, as they take the form of first-order hyperbolic balance laws. The first-order nature of the models has been shown to greatly increase the robustness of numerical solution of lower quality meshes [11], as compared to the numerical solution of the Navier-Stokes equations. These moment equations do, however, often have stiff local source terms. Fortunately, as the source terms are entirely local, they do not add global stiffness to the problem. Point-implicit time-marching methods can be used to efficiently advance numerical solutions.

In this work, the DGH method is selected. This numerical scheme was developed by Suzuki and van Leer [13] specifically for the efficient and accurate solution of moment equations. It is based on the upwind moment scheme of Huynh [22], and extends the method for the efficient solution of hyperbolic laws with stiff local sources. Somewhat remarkably, this coupled space-time method achieves third-order accuracy in both space and time, while only using linear elements [23, 24, 14]. The DGH method can be implemented in a highly efficient manner for execution in parallel computational resources, as neighbouring cells only need to exchange information once per time step. Also, the time-step stability limit for the DGH method is far less restrictive than that of traditional high-order Runge-Kutta-DG methods, meaning larger time steps can safely be taken. The result is that the scheme can easily achieve extremely high parallel efficiency, even when hundreds of thousands of cores are used, as demonstrated in [14]. It is also very amenable to implementation on unstructured grids or when adaptive mesh refinement (AMR) is used.

In the DGH scheme, each moment member of the conserved solution vector,  $\mathbf{U}(x_j, t)|_{\Omega_k}$ , in Eq. (5) and Eq. (11) is assumed to be a linear polynomial function over the domain of each grid element  $\Omega_k$ . Moreover, the space of scalar test functions in this Galerkin formulation is taken to be the same as the space for the solution, yielding

$$\mathbf{U}(x_j, t)|_{\Omega_k}, \nu(x_j)|_{\Omega_k} \in P^1(\Omega_k), \tag{13}$$

where  $x_j = [x, y, z]$  is a position vector in a Cartesian coordinate system and

$$\begin{aligned}
P^1(\Omega_k) &= \text{span} \{ \phi_0(x_j), \phi_1(x_j), \phi_2(x_j), \phi_3(x_j) \} \\
&= \text{span} \{ 1, x - x_{c_k}, y - y_{c_k}, z - z_{c_k} \}.
\end{aligned} \tag{14}$$

Here,  $\mathbf{x}_{c_k} = [x_{c_k}, y_{c_k}, z_{c_k}]$  is the centroid of the element  $\Omega_k$ . Thus, the numerical solution for a particular computational element  $k$  is taken as

$$\mathbf{U}_k = \bar{\mathbf{U}}_k + (\overline{\Delta_x \mathbf{U}})_k (x - x_{c_k}) + (\overline{\Delta_y \mathbf{U}})_k (y - y_{c_k}) + (\overline{\Delta_z \mathbf{U}})_k (z - z_{c_k}), \quad (15)$$

where  $\bar{\mathbf{U}}_k$  is the cell solution average, and  $(\overline{\Delta_x \mathbf{U}})_k$ ,  $(\overline{\Delta_y \mathbf{U}})_k$ , and  $(\overline{\Delta_z \mathbf{U}})_k$  are the components of the solution gradient in the  $x$ ,  $y$ , and  $z$  Cartesian directions, respectively. These solution variables represent the degrees of freedom for which the equations of the ten-moment model, Eq.(11), are solved for.

The *weak* form of Eq. (5) for an element  $\Omega_k$  is obtained by applying a Galerkin approach [13], which after performing integration by parts yields

$$\begin{aligned} \int_{\Omega_k} \nu(x_j) [\mathbf{U}^{n+1} - \mathbf{U}^n] dx_j = & - \iint_{\Gamma_k \times T} \nu(x_j) \mathbf{F}_i \cdot \hat{n}_i d\Gamma dt + \iint_{\Omega_k \times T} \mathbf{F}_i \frac{\partial}{\partial x_i} \nu(x_j) dx_j dt \\ & + \iint_{\Omega_k \times T} \nu(x_j) \mathbf{S} dx_j dt, \end{aligned} \quad (16)$$

where  $T$  is the time interval over  $[t^n, t^{n+1}]$ .

Inserting the solution representation given by Eq. (15) into the weak formulation, Eq. (16), and performing integration using each test function yield update formulas for the solution degrees of freedom (i.e., cell solution average and slopes). The right-hand side of the update equations contains five integrals defined over coupled space-time domains [13, 14]: i) two surface integrals for the boundary flux through the coupled space-time surface of the computational element, ii) a flux volumetric integral, and iii) two volumetric integrals for the source term. Since the local source term is stiff, the Radau IIA method is used for time integration, which leads to solution update formulas at time  $t^{n+\frac{1}{3}}$  and  $t^{n+1}$ . Finally, the application of the Gaussian quadrature rule for space domain integration, and the use of Hancock's predictor step for the solution evaluation at the half time steps,  $\mathbf{U}_h(x_i, t^{n+\frac{1}{2}})$  and  $\mathbf{U}_h(x_i, t^{n+\frac{1}{6}})$ , yield the following discrete formulas for the solution cell-average and slope updates (see [13, 14] for details):

$$\begin{bmatrix} \bar{\mathbf{U}}_k^{n+\frac{1}{3}} \\ \bar{\mathbf{U}}_k^{n+1} \end{bmatrix} = \begin{bmatrix} \bar{\mathbf{U}}_k^n \\ \bar{\mathbf{U}}_k^n \end{bmatrix} - \frac{\Delta t}{V_k} \begin{bmatrix} \frac{1}{3} \sum_{\xi} w_{\xi} \tilde{\mathbf{F}}_{\xi}^{n+\frac{1}{6}} \\ \xi \\ \sum_{\xi} w_{\xi} \tilde{\mathbf{F}}_{\xi}^{n+\frac{1}{2}} \end{bmatrix} + \Delta t \begin{bmatrix} \frac{5}{12} \mathbf{I} & -\frac{1}{12} \mathbf{I} \\ \frac{3}{4} \mathbf{I} & \frac{1}{4} \mathbf{I} \end{bmatrix} \begin{bmatrix} \bar{\mathbf{S}}^{n+\frac{1}{3}} \\ \bar{\mathbf{S}}^{n+1} \end{bmatrix}, \quad (17)$$

$$\begin{aligned} \begin{bmatrix} \overline{\Delta_x \mathbf{U}}_k^{n+\frac{1}{3}} \\ \overline{\Delta_y \mathbf{U}}_k^{n+\frac{1}{3}} \\ \overline{\Delta_z \mathbf{U}}_k^{n+\frac{1}{3}} \\ \overline{\Delta_x \mathbf{U}}_k^{n+1} \\ \overline{\Delta_y \mathbf{U}}_k^{n+1} \\ \overline{\Delta_z \mathbf{U}}_k^{n+1} \end{bmatrix} &= \begin{bmatrix} \overline{\Delta_x \mathbf{U}}_k^n \\ \overline{\Delta_y \mathbf{U}}_k^n \\ \overline{\Delta_z \mathbf{U}}_k^n \\ \overline{\Delta_x \mathbf{U}}_k^n \\ \overline{\Delta_y \mathbf{U}}_k^n \\ \overline{\Delta_z \mathbf{U}}_k^n \end{bmatrix} + \Delta t \mathbf{Y} \begin{bmatrix} \frac{1}{3} \sum_{\xi} w_{\xi} \Delta x_{\xi} \tilde{\mathbf{F}}_{\xi}^{n+\frac{1}{6}} \\ \frac{1}{3} \sum_{\xi} w_{\xi} \Delta y_{\xi} \tilde{\mathbf{F}}_{\xi}^{n+\frac{1}{6}} \\ \frac{1}{3} \sum_{\xi} w_{\xi} \Delta z_{\xi} \tilde{\mathbf{F}}_{\xi}^{n+\frac{1}{6}} \\ \sum_{\xi} w_{\xi} \Delta x_{\xi} \tilde{\mathbf{F}}_{\xi}^{n+\frac{1}{2}} \\ \sum_{\xi} w_{\xi} \Delta y_{\xi} \tilde{\mathbf{F}}_{\xi}^{n+\frac{1}{2}} \\ \sum_{\xi} w_{\xi} \Delta z_{\xi} \tilde{\mathbf{F}}_{\xi}^{n+\frac{1}{2}} \end{bmatrix} + \Delta t \mathbf{Y} \begin{bmatrix} \frac{1}{3} \sum_{\chi} w_{\chi} |\mathbf{J}(\zeta_j)| \left[ \frac{1}{2} (\mathbf{F}_x)_{\chi}^n + \frac{1}{2} (\mathbf{F}_x)_{\chi}^{n+\frac{1}{3}} \right] \\ \frac{1}{3} \sum_{\chi} w_{\chi} |\mathbf{J}(\zeta_j)| \left[ \frac{1}{2} (\mathbf{F}_y)_{\chi}^n + \frac{1}{2} (\mathbf{F}_y)_{\chi}^{n+\frac{1}{3}} \right] \\ \frac{1}{3} \sum_{\chi} w_{\chi} |\mathbf{J}(\zeta_j)| \left[ \frac{1}{2} (\mathbf{F}_z)_{\chi}^n + \frac{1}{2} (\mathbf{F}_z)_{\chi}^{n+\frac{1}{3}} \right] \\ \sum_{\chi} w_{\chi} |\mathbf{J}(\zeta_j)| \left[ \frac{3}{4} (\mathbf{F}_x)_{\chi}^{n+\frac{1}{3}} + \frac{1}{4} (\mathbf{F}_x)_{\chi}^{n+1} \right] \\ \sum_{\chi} w_{\chi} |\mathbf{J}(\zeta_j)| \left[ \frac{3}{4} (\mathbf{F}_y)_{\chi}^{n+\frac{1}{3}} + \frac{1}{4} (\mathbf{F}_y)_{\chi}^{n+1} \right] \\ \sum_{\chi} w_{\chi} |\mathbf{J}(\zeta_j)| \left[ \frac{3}{4} (\mathbf{F}_z)_{\chi}^{n+\frac{1}{3}} + \frac{1}{4} (\mathbf{F}_z)_{\chi}^{n+1} \right] \end{bmatrix} \\ &+ \mathbf{S}, \end{aligned} \quad (18)$$

$$\mathcal{S} = \Delta t \begin{bmatrix} \frac{5}{12} \mathbf{I} & -\frac{1}{12} \mathbf{I} \\ \frac{3}{4} \mathbf{I} & \frac{1}{4} \mathbf{I} \end{bmatrix} \begin{bmatrix} \frac{\partial \mathbf{S}^{n+\frac{1}{3}}}{\partial \bar{U}} \overline{\Delta_x \mathbf{U}_k^{n+\frac{1}{3}}} \\ \frac{\partial \mathbf{S}^{n+\frac{1}{3}}}{\partial \bar{U}} \overline{\Delta_y \mathbf{U}_k^{n+\frac{1}{3}}} \\ \frac{\partial \mathbf{S}^{n+\frac{1}{3}}}{\partial \bar{U}} \overline{\Delta_z \mathbf{U}_k^{n+\frac{1}{3}}} \\ \frac{\partial \mathbf{S}^{n+1}}{\partial \bar{U}} \overline{\Delta_x \mathbf{U}_k^{n+1}} \\ \frac{\partial \mathbf{S}^{n+1}}{\partial \bar{U}} \overline{\Delta_y \mathbf{U}_k^{n+1}} \\ \frac{\partial \mathbf{S}^{n+1}}{\partial \bar{U}} \overline{\Delta_z \mathbf{U}_k^{n+1}} \end{bmatrix}. \quad (19)$$

Here, the following quantities are used:  $\Delta \zeta_\xi = \zeta_\xi - \zeta_{c_k}$  is the distance along a particular coordinate  $\zeta$  between an arbitrary Gaussian boundary point with index  $\xi$  and the cell centroid of element  $\Omega_k$ ,  $w_\xi$  is the Gaussian weight,  $\mathbf{J}(\zeta_j)$  is the Jacobian of the trilinear transformation mapping the hexahedral element  $\Omega_k$  to a canonical cube,  $\chi$  index denotes volumetric Gaussian points, and  $\mathbf{K}_k$  and  $\mathbf{Y}$  matrices are given by

$$\mathbf{K}_k = \begin{bmatrix} I_{xx} & I_{xy} & I_{xz} \\ I_{yx} & I_{yy} & I_{yz} \\ I_{zx} & I_{zy} & I_{zz} \end{bmatrix}^{-1}, \quad \mathbf{Y} = \begin{bmatrix} \mathbf{K}_k & \mathbf{0} & \mathbf{0} \\ \mathbf{0} & \mathbf{K}_k & \mathbf{0} \\ \mathbf{0} & \mathbf{0} & \mathbf{K}_k \end{bmatrix}, \quad (20)$$

where  $I_{\xi\zeta} = \iiint_{\Omega_k} (\xi - \xi_{c_k})(\zeta - \zeta_{c_k}) dx_j$  is the product moment of area for  $\xi$  and  $\zeta$  axes.  $\mathbf{I} \in \mathbb{R}^{3 \times 3}$  is the identity matrix.  $\tilde{\mathbf{F}}_\xi$  is the vector of computed fluxes normal to the element edge  $\partial\Gamma_k$ , and is computed here by using the Harten-Lax-Leer-Einfeldt (HLLC) approximate Riemann flux function [25].

## 5 Taylor-Green Vortex Problem

To demonstrate the ability of the ten-moment model described in Sect. 3.2 to perform the DNS of turbulent flow, the Taylor–Green vortex problem is considered.

The TGV is a synthetic flow field that has been widely used for performing the DNS of turbulent flow. An exact initial condition can be specified which is an infinite periodic array of vortices having counter-rotating neighbors, thereby allowing comparisons of different solution methods. In three dimensions, vortex stretching occurs and energy is transported from large scales to smaller scales, such that new small-scale vortices appear, while the base vortex decays. This cascading process leads the flow to transition to turbulence, followed by a subsequent decay phase similar to homogeneous isotropic turbulence.

The TGV benchmark has been used in connection with many numerical methods, including high-order discontinuous-Galerkin methods, flux reconstruction schemes, different variants of the lattice Boltzmann method, and DSMC (see [3, 6, 7, 8, 26, 27, 28, 29, 30, 31] and the references therein). This flow problem was one of the cases considered in all first five international workshops on high-order CFD (computational fluid dynamics) methods, including as a challenging test in the first three.

The test case of a three-dimensional (3D) TGV at the Reynolds number of 1,600 and Mach number of 0.1 is chosen here as this specific test case is well studied, and reference solutions based on the NS equations for energy decay, enstrophy evolution and energy spectra are readily available from the literature. Note that for this particular flow conditions, reference data are not only available for the increasing enstrophy but also for decaying enstrophy. As described in [6], the 3D incompressible NS equations with constant physical properties are typically used as the governing equations for this flow. Additionally, the temperature field does not need to be computed. Alternatively, the 3D compressible NS equations at low Mach number can be used for the simulation of this test case.

For the present study, we follow the setup of Wang *et al.* [6] which was also used by Jacobs *et al.* [27]. The flow is solved in a periodic domain given by  $(x, y, z) \in [0, 2\pi L]^3$ , with a non-dimensional reference length  $L = 1$ . The initial condition is given by the set of primitive variables  $\mathbf{W}_0 = [\rho, u_x, u_y, u_z, p]^T$  which is taken

as

$$\mathbf{W}_0 = \begin{bmatrix} \rho \\ V \sin\left(\frac{x}{L}\right) \cos\left(\frac{y}{L}\right) \cos\left(\frac{z}{L}\right) \\ -V \cos\left(\frac{x}{L}\right) \sin\left(\frac{y}{L}\right) \cos\left(\frac{z}{L}\right) \\ 0 \\ \frac{1}{\gamma M^2} + \frac{1}{16} \left[ \cos\left(\frac{2x}{L}\right) + \cos\left(\frac{2y}{L}\right) \right] \left[ \cos\left(\frac{2z}{L}\right) + 2 \right] \end{bmatrix}. \quad (21)$$

Here, the non-dimensional velocity  $V = 1$ , and density is computed with the equation of state  $\rho = \frac{\gamma p M^2}{T_{\text{ref}}}$  using a reference temperature  $T_{\text{ref}} = 1$  and a Mach number of  $M = 0.1$ . The Reynolds number of the flow is defined as  $\text{Re} = \frac{\rho_{\text{ref}} V L}{\mu}$ , and is equal to 1,600. The reference density is taken to be  $\rho_{\text{ref}} = 1$ , and the appropriate viscosity is then  $\mu = 1/1,600$ , with the bulk viscosity approximated as  $\mu_B = 3\mu$ . Figure 1a depicts the initial variation for the velocity and vorticity magnitudes for this problem.

In the present study, the solution is time-marched to final non-dimensional time  $t = 20$ , using a CFL (Courant–Friedrichs–Lewy) number of 0.1 for all mesh resolutions considered. The HLLC flux function and no slope limiter were used. Computational studies have been performed with the DGH scheme on a series of Cartesian meshes ranging in size from  $128^3$  to  $512^3$  uniform elements for a total of 2,097,152 and 134,217,728 cells, respectively. Figures 1b to 1e show 3D contour plots of the predicted instantaneous velocity and vorticity magnitudes obtained on the  $512^3$  Cartesian grid at the time instances  $t = 2.5, 9.0, 15.0$  and  $17.5$ , respectively. Note that the vorticity magnitude is plotted along 30 Q-isosurfaces equally distributed across the instantaneous range of positive Q values. As discussed in [32], positive Q isosurfaces isolate areas where the strength of rotation overcomes the strain, thus making those surfaces eligible as vortex envelopes.

To validate the results, the temporal evolution of certain integrated quantities has been compared against the reference data from Wang *et al.* [6], which was obtained by solving the incompressible NS equations on a grid with  $512^3$  elements using a spectral method. Specifically, the integrals of the kinetic energy and enstrophy for the entire domain  $\Omega$ ,

$$E_k = \frac{1}{\rho_{\text{ref}} \Omega} \int_{\Omega} \frac{1}{2} \rho u_j u_j \, d\Omega, \quad \text{and} \quad (22a)$$

$$\mathcal{E} = \frac{1}{\rho_{\text{ref}} \Omega} \int_{\Omega} \frac{1}{2} \rho |\nabla \times \vec{u}|^2 \, d\Omega, \quad (22b)$$

respectively, have been computed by performing accurate Gaussian quadrature integration for the integrands, which were evaluated with the predicted DGH solution and solution gradient (see Eq. 15). Additionally, the temporal evolution of the kinetic energy dissipation rate,  $\epsilon = -\frac{dE_k}{dt}$ , can be related to the enstrophy exactly for incompressible flows as

$$\mathcal{E} = \frac{\rho_{\text{ref}} \epsilon}{2\mu}, \quad (23)$$

and this expression holds also approximately true for compressible flows at low Mach number.

Figure 2a depicts the predicted temporal evolution of the kinetic energy on three uniformly refined Cartesian meshes with  $128^3$ ,  $256^3$ , and  $512^3$  elements. As the grid is refined, it is quite obvious that the kinetic energy predicted by the DGH scheme approaches the spectral prediction of Wang *et al.* [6] on  $512^3$  elements. An inspection of Fig. 2a shows that the 3rd-order DGH solution appears to be converging towards the reference data, although some slight differences can still be noticed at the end of the dissipation dominated phase (i.e., beyond about  $t = 15$ ).

The temporal variation of enstrophy,  $\mathcal{E}$ , has also been examined based on both evaluation formulas, and the results are depicted in Fig. 2b. The direct evaluation of enstrophy, referred to as ‘‘DGH’’ in the figure, uses Eq. 22b and the DGH solution slopes to compute the flow vorticity. To evaluate enstrophy based on Eq. 23, denoted as ‘‘DGH,  $E_k$ -solution based’’ in Fig. 2b, a 4th-order finite-difference approximation for the

time derivative of the kinetic energy variation depicted in Fig. 2a has been used. The examination of Fig. 2b reveals that, as in the case of kinetic energy, the predicted enstrophy variation by the DGH scheme converges towards the spectral prediction [6] as the mesh is refined. However, in contrast to the observed behaviour for the kinetic energy, the estimated enstrophy computed directly with the solution slopes predicted by the DGH scheme is approaching the reference data at a relatively slower rate. Nevertheless, the indirect estimation of the enstrophy based on numerical differentiation of  $E_k$  temporal variation reveals significantly improved predictions that are much closer to the reference data. This behaviour can be explained by considering that the enstrophy relies on derivatives of the velocity field whereas the kinetic energy depends directly on the velocity field. Recalling that the 3rd-order DGH scheme relies on linear elements for the solution procedure (see Eq. 15), it is obvious that the solution slopes are approximated with lower accuracy than the solution, and this fact is reflected in the direct evaluation of the enstrophy in this case.

Although the  $E_k$ -solution-based enstrophy approach the reference solution as the mesh is refined, the prediction on the most refined grid does not fully agree with the continuum result, and the differences between the two curves are more significant than in the case of kinetic energy. A first plausible explanation for these differences is that the DGH solution is still not fully converged, considering that the comparison is performed between the prediction of a 3rd-order scheme versus that of a spectral method for the same grid resolution, with the latter being obviously more accurate. Although no definite conclusion can be made about the numerical convergence of the DGH result on the finest resolution, an inspection of the Kolmogorov scale for this problem [31] at the time when the enstrophy peaks, i.e.,  $t = 9.0$ , reveals that it is on the order of the cell length. Furthermore, the Knudsen number of that scale, based on our results, is approximately 0.008 which corresponds to regimes at which non-equilibrium effects begin to be observed. Therefore, it is conceivable that the differences might persist even as the mesh is further refined, and be deemed as modelling differences between the continuum fluid representation used in the Navier-Stokes equations and the extended hydrodynamics formulation provided by the moment method. To elucidate the exact nature of the observed differences additional high-resolution studies and analyses of this case would be required.

## 6 Conclusions

The present work has demonstrated that the ten-moment (Gaussian) closure model for viscous, compressible fluid flow can be used for the DNS of turbulent flow. To the best of our knowledge, this is the first application of hyperbolic moment-models to this type of simulations.

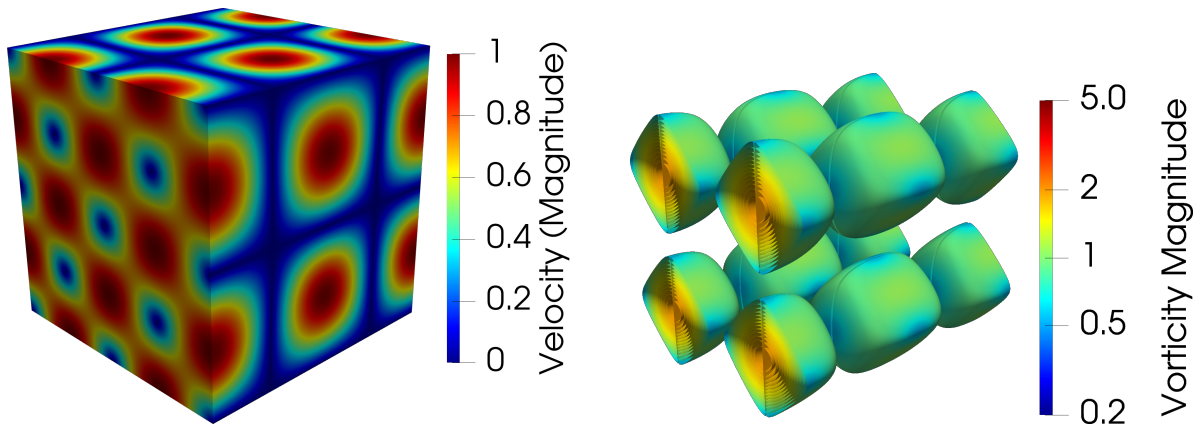
The DGH scheme proved to be a key enabler of this work by providing third-order solution accuracy with only linear elements, an efficient treatment for the stiff local source terms in the ten-moment model, and allowing the development of an efficient, large-scale computational framework for execution on massively parallel architectures [14]. The results presented for Taylor-Green vortex problem demonstrate that the 3rd-order DGH method is able to resolve small-scale structures accurately in the DNS of a turbulent flow.

Comparisons against the spectral data of Wang *et al.* [6] for the TGV problem, show that the DGH prediction on the most refined grid does not fully agree with the continuum result. The differences in the predicted temporal evolution of the kinetic energy are relatively minor, but more significant differences are observed in the predicted temporal evolution of the enstrophy. Although no definite conclusion can be made about the numerical convergence of the DGH result, the determined Knudsen number at Kolmogorov scale shows that the differences might potentially occur due non-equilibrium effects. Further investigations are required to elucidate the observed discrepancies.

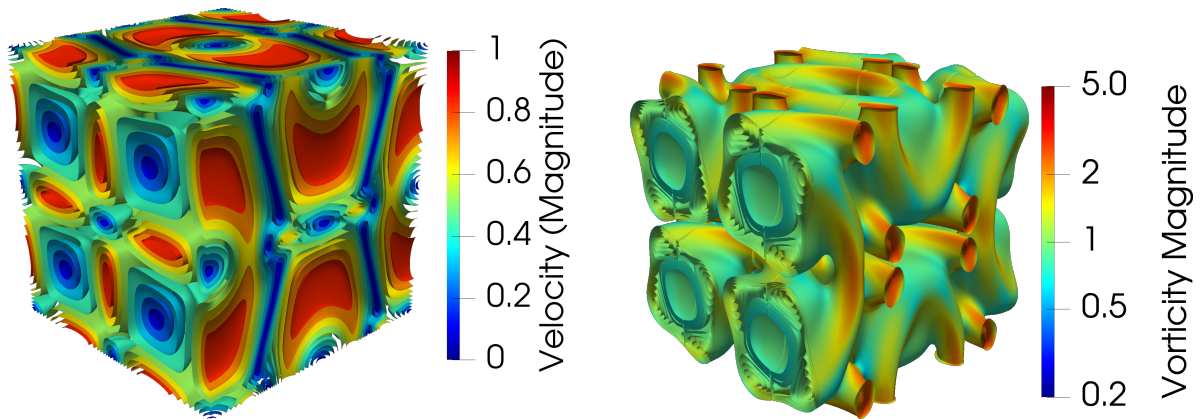
The moment-based approach provides an extended hydrodynamics model that is not only valid beyond the continuum regime of the fluid flow, but also is more computationally affordable than DSMC for certain non-equilibrium flow regimes. Thus, the approach proposed in the present work could also be used for the investigation of non-continuum effects that might be present at Kolmogorov scale for turbulent flows, as theoretically predicted and recently observed in numerical experiments.

## Acknowledgments

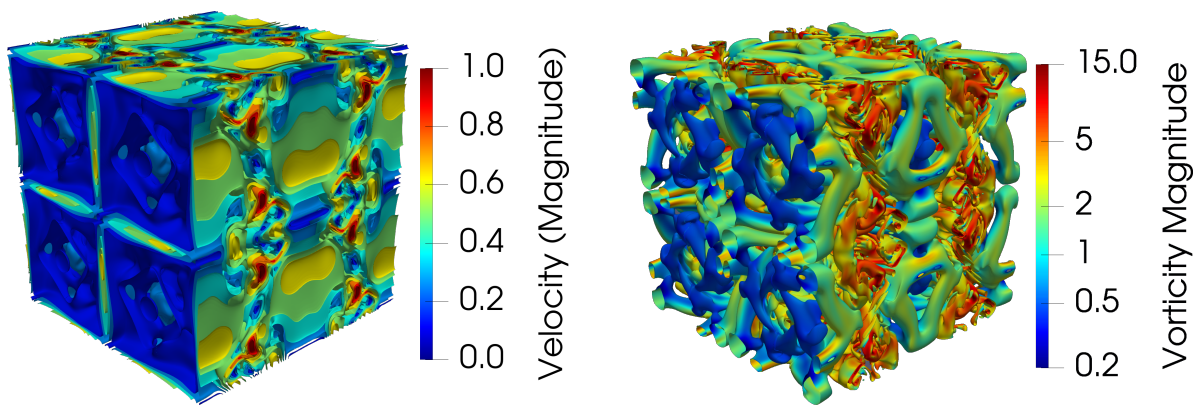
The authors would like to express gratitude to Prof. J.G. McDonald of University of Ottawa for his fruitful discussions and guidance provided to this research.



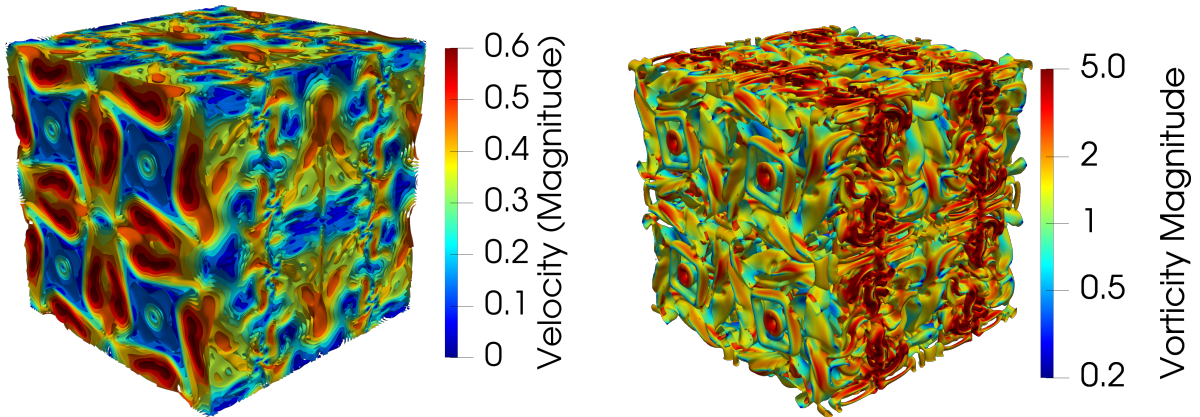
(a)  $t = 0.0$ .



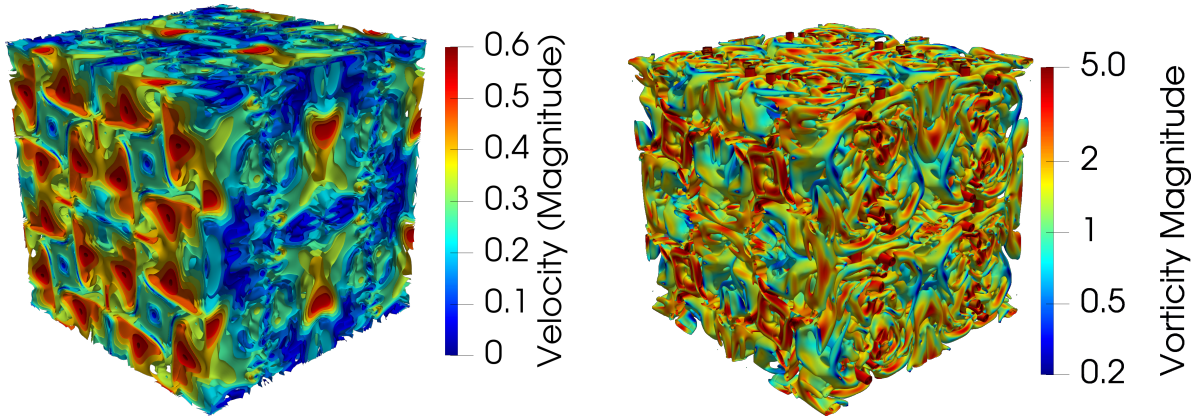
(b)  $t = 2.5$ .



(c)  $t = 9.0$ .



(d)  $t = 15.0$ .



(e)  $t = 17.5$ .

Figure 1: Contour plots of the magnitude of velocity (left) and vorticity (right) for the TGV problem at various non-dimensional times. The solutions are predicted by solving the ten-moment model with the DGH scheme on a Cartesian grid with  $512^3$  elements. The vorticity magnitude is plotted along a number of  $Q$ -isosurfaces equally distributed across the instantaneous range of positive  $Q$  values. The number of isosurfaces is 15 for the solution at  $t = 0.0$  and 30 for the rest of the time instances.

This study was funded by the Natural Science and Engineering Research Council of Canada (NSERC) through grant number RGPIN-2020-06295 and by the Atomic Energy of Canada Limited, under the auspices of the Federal Nuclear Science and Technology Program. The research was conducted at the Canadian Nuclear Laboratories. Computational resources for this work were provided by the Argonne Leadership Computing Facility (ALCF) and the Niagara supercomputer at the SciNet HPC Consortium. The ALCF is a DOE Office of Science User Facility supported under Contract DE-AC02-06CH11357. The SciNet HPC consortium is funded by the Canada Foundation for Innovation; the Government of Ontario; Ontario Research Fund - Research Excellence; and the University of Toronto [33, 34]. The authors are very grateful for this support.

## References

- [1] D.C. Wilcox. *Turbulence Modeling for CFD*. DCW Industries, 2006.
- [2] R.D. Moser. On the validity of the continuum approximation in high Reynolds number turbulence. *Phys. Fluids*, 18:078105, 2006.

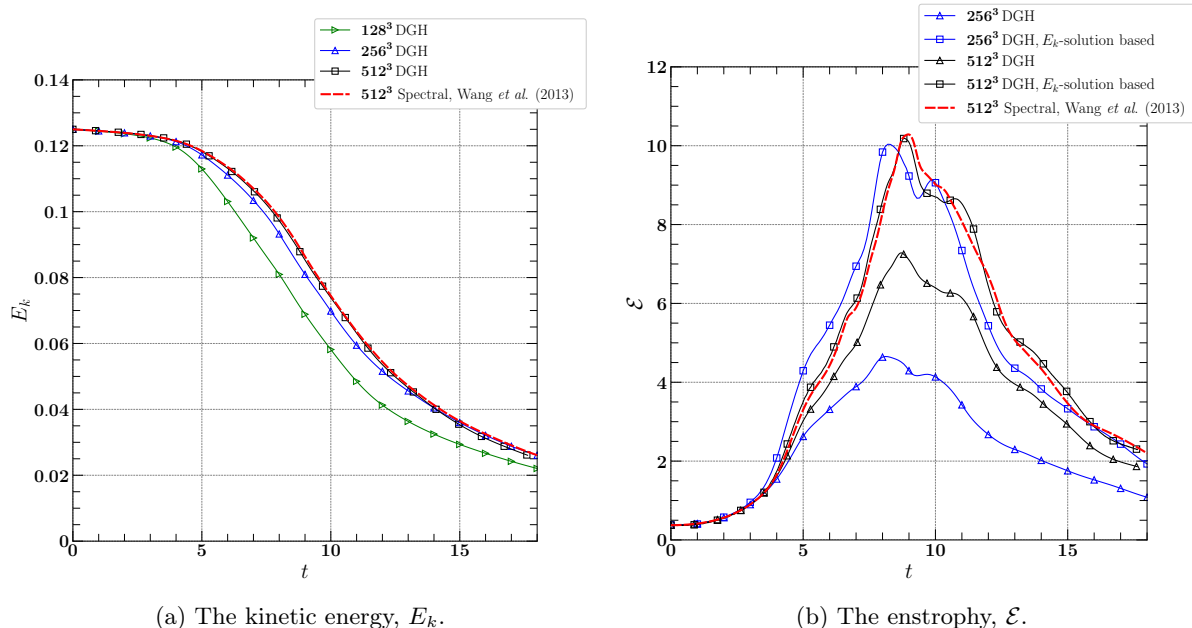


Figure 2: Plot of the predicted kinetic energy and enstrophy by the DGH scheme along with the reference spectral method solution from Wang *et al.* [6].

- [3] M. A. Gallis, N. P. Bitter, T. P. Koehler, J. R. Torczynski, S. J. Plimpton, and G. Papadakis. Molecular-level simulations of turbulence and its decay. *Phys. Rev. Lett.*, 118:064501, Feb 2017.
- [4] T. I. Gombosi. *Gaskinetic Theory*. Cambridge University Press, Cambridge, 1994.
- [5] Thomas B. Gatski and Jean-Paul Bonnet. *Compressibility, Turbulence and High Speed Flow*. Elsevier, 2013.
- [6] Z.J. Wang, Krzysztof Fidkowski, Rémi Abgrall, Francesco Bassi, Doru Caraeni, Andrew Cary, Herman Deconinck, Ralf Hartmann, Koen Hillewaert, H.T. Huynh, Norbert Kroll, Georg May, Per-Olof Persson, Bram van Leer, and Miguel Visbal. High-order CFD methods: current status and perspective. *International Journal for Numerical Methods in Fluids*, 72(8):811–845, 2013.
- [7] M. A. Gallis, J. R. Torczynski, M. C. Krygier, N. P. Bitter, and S. J. Plimpton. Turbulence at the edge of continuum. *Phys. Rev. Fluids*, 6:013401, Jan 2021.
- [8] Ryan M. McMullen, Michael C. Krygier, John R. Torczynski, and Michael A. Gallis. Navier-stokes equations do not describe the smallest scales of turbulence in gases. *Phys. Rev. Lett.*, 128:114501, Mar 2022.
- [9] C. D. Levermore. Moment closure hierarchies for kinetic theories. *J. Stat. Phys.*, 83:1021–1065, 1996.
- [10] C. David Levermore and William J. Morokoff. The Gaussian moment closure for gas dynamics. *SIAM J. Appl. Math.*, 59(1):72–96, 1998.
- [11] J. G. McDonald, J. S. Sachdev, and C. P. T. Groth. Application of Gaussian moment closure to micro-scale flows with moving and embedded boundaries. *AIAA J.*, 52(9):1839–1857, 2014.
- [12] J. Hittinger. *Foundations for the generalization of the Godunov method to hyperbolic systems with stiff relaxation source terms*. PhD thesis, University of Michigan, 2000.
- [13] Y. Suzuki. *Discontinuous Galerkin Methods for Extended Hydrodynamics*. PhD thesis, University of Michigan, 2008.
- [14] W. Kaufmann and J.G. McDonald. Large-scale investigation of 3D discontinuous-Galerkin Hancock method for hyperbolic balance laws with stiff local sources. In *the 11th Proceedings of the International Conference on Computational Fluid Dynamics, Maui, Hawaii, USA, July 11-15, 2022*. Paper ICCFD11-2022-0501.
- [15] H. Grad. On the kinetic theory of rarefied gases. *Commun. Pure Appl. Math.*, 2:331–407, 1949.
- [16] W. Dreyer. Maximization of the entropy in non-equilibrium. *Journal of Physics A: Mathematical and*

- General*, 20:6505–6517, 1987.
- [17] I. Müller and T. Ruggeri. *Extended Thermodynamics*. Springer-Verlag, New York, 1993.
  - [18] S. L. Brown, P. L. Roe, and C. P. T. Groth. Numerical solution of a 10-moment model for nonequilibrium gasdynamics. Paper 95-1677, AIAA, June 1995.
  - [19] S. L. Brown. *Approximate Riemann Solvers for Moment Models of Dilute Gases*. PhD thesis, University of Michigan, 1996.
  - [20] J. McDonald and C. P. T. Groth. Numerical modeling of micron-scale flows using the Gaussian moment closure. Paper 2005-5035, AIAA, June 2005.
  - [21] T. J. Barth. On discontinuous Galerkin approximations of Boltzmann moment systems with Levermore closure. *Comp. Meth. Appl. Mech. Eng.*, 195:3311–3330, 2006.
  - [22] H.T. Huynh. An upwind moment scheme for conservation laws. In *Computational Fluid Dynamics 2004*, pages 761–766. Springer, 2006.
  - [23] A. Miri and J. G. McDonald. A discontinuous-Galerkin-Hancock method for viscous CFD and multi-phase flows using first-order PDEs. In *Proceedings of the 10th International Conference on Computational Fluid Dynamics (ICCFD10), Valencia Spain, July 9–13, 2018*.
  - [24] W. Kaufmann, L. Ivan, and J. G. McDonald. Extended hydrodynamics using the discontinuous-Galerkin-Hancock method. In *Proceedings of the 29th Annual Conference of the CFD Society of Canada, Online, July 27–29, 2021*.
  - [25] B. Einfeldt. On Godunov-type methods for gas dynamics. *SIAM J. Numer. Anal.*, 25:294–318, 1988.
  - [26] *Case 3.3: Taylor-Green Vortex Evolution*, 2015.
  - [27] Christian T. Jacobs, Satya P. Jammy, and Neil D. Sandham. Opensbli: A framework for the automated derivation and parallel execution of finite difference solvers on a range of computer architectures. *Journal of Computational Science*, 18:12–23, 2017.
  - [28] David Flad, Andrea Beck, and Claus-Dieter Munz. Simulation of underresolved turbulent flows by adaptive filtering using the high order discontinuous Galerkin spectral element method. *Journal of Computational Physics*, 313:1–12, 2016.
  - [29] J. R. Bull and A. Jameson. Simulation of the Taylor–Green vortex using high-order flux reconstruction schemes. *AIAA J.*, 53(9):2750–2761, 2015.
  - [30] Marian Piatkowski, Steffen Müthing, and Peter Bastian. A stable and high-order accurate discontinuous Galerkin based splitting method for the incompressible Navier–Stokes equations. *Journal of Computational Physics*, 356:220–239, 2018.
  - [31] Martin Geier, Stephan Lenz, Martin Schönherr, and Manfred Krafczyk. Under-resolved and large eddy simulations of a decaying Taylor–Green vortex with the cumulant lattice Boltzmann method. *Theor. Comput. Fluid Dyn.*, 35:169–208, 2021.
  - [32] Yves Dubief and Franck Delcayre. On coherent-vortex identification in turbulence. *Journal of Turbulence*, 1:N11, 2000.
  - [33] M. Ponce, R. van Zon, S. Northrup, D. Gruner, J. Chen, F. Ertinaz, A. Fedoseev, L. Groer, F. Mao, B. C. Mundim, M. Nolta, J. Pinto, M. Saldarriaga, V. Slavic, E. Spence, C.-H. Yu, and W. R. Peltier. Deploying a Top-100 supercomputer for large parallel workloads: the Niagara supercomputer. In *PEARC '19: Proceedings of the Practice and Experience in Advanced Research Computing on Rise of the Machines (learning)*, 2019.
  - [34] C. Loken, D. Gruner, L. Groer, R. Peltier, N. Bunn, M. Craig, T. Henriques, J. Dempsey, C.-H. Yu, J. Chen, L. J. Dursi, J. Chong, S. Northrup, J. Pinto, N. Knecht, and R. van Zon. SciNet: Lessons learned from building a power-efficient Top-20 system and data centre. In *J. Phys.: Conf. Ser.*, 2010.